Journal of Applied Physics ARTICLE scitation.org/journal/jap

From atomistic tight-binding theory to macroscale drift–diffusion: Multiscale modeling and numerical simulation of uni-polar charge transport in (In,Ga)N devices with random fluctuations

Cite as: J. Appl. Phys. **130**, 065702 (2021); doi: 10.1063/5.0059014
Submitted: 4 June 2021 · Accepted: 23 July 2021 ·
Published Online: 10 August 2021

Michael O'Donovan,[1,2,a)] Debapriya Chaudhuri,[1] Timo Streckenbach,[3] Patricio Farrell,[3,b)] Stefan Schulz,[1] and Thomas Koprucki[3]

AFFILIATIONS

[1]Tyndall National Institute, University College Cork, Cork T12 R5CP, Ireland
[2]Department of Physics, University College Cork, Cork T12 YN60, Ireland
[3]Weierstrass Institute (WIAS), Mohrenstr. 39, 10117 Berlin, Germany

Note: This paper is part of the Special Topic on Wide Bandgap Semiconductor Materials and Devices.
[a)]**Author to whom correspondence should be addressed:** michael.odonovan@tyndall.ie
[b)]patricio.farrell@wias-berlin.de

ABSTRACT

Random alloy fluctuations significantly affect the electronic, optical, and transport properties of (In,Ga)N-based optoelectronic devices. Transport calculations accounting for alloy fluctuations currently use a combination of modified continuum-based models, which neglect to a large extent atomistic effects. In this work, we present a model that bridges the gap between atomistic theory and macroscopic transport models. To do so, we combine atomistic tight-binding theory and continuum-based drift–diffusion solvers, where quantum corrections are included via the localization landscape method. We outline the ingredients of this framework in detail and present first results for uni-polar electron transport in single and multi- (In,Ga)N quantum well systems. Overall, our results reveal that both random alloy fluctuations and quantum corrections significantly affect the current–voltage characteristics of uni-polar electron transport in such devices. However, our investigations indicate that the importance of quantum corrections and random alloy fluctuations can be different for single and multi-quantum well systems.

I. INTRODUCTION

III-nitride (III-N)-based quantum well (QW) structures are at the heart of modern short wavelength light emitting diodes (LEDs).[1,2] Here, (In,Ga)N/GaN multi-QWs (MQWs) are used to realize devices operating in the visible part of the spectrum. While in the blue wavelength range such III-N LEDs offer very high efficiencies, achieving the same at longer wavelengths is very challenging. Therefore, to tailor and guide the design of future energy efficient III-N LED structures operating over a wide spectral range, accurately modeling their fundamental properties is essential.

It is important to note that nitride-based heterostructures have in general very different properties to other III–V material systems, such as GaAs or AlGaAs. This starts with the underlying crystal structure: the thermodynamically stable phase for GaAs is zinc blende, while III-N systems preferentially crystallize in the wurtzite phase.[3–5] This difference in the crystal structure has far reaching consequences, resulting, for instance, in a spontaneous electric polarization vector field in wurtzite III-N systems; such a field is absent in a zinc blende structure.[6] Therefore, in a nitride-based heterostructure, any discontinuity in the polarization vector field leads to a very strong electrostatic built-in field, which then can give rise

to a quantum confined Stark effect (QCSE).[7,8] The QCSE is further increased by strain dependent piezoelectric polarization contributions.[9,10] As a consequence, the radiative recombination rates in III-N heterostructures are strongly reduced by the QCSE.[7,11,12]

When it comes to modeling charge carrier transport in LED structures utilizing III-N QWs, the effects of the built-in polarization field are taken into account in "standard" one-dimensional (1D) drift–diffusion (DD) simulations. However, in general, the turn-on voltages predicted by such an approach are considerably higher compared to experiments.[13–15] It has recently been shown that this shortcoming in the simulation of (In,Ga)N-based LEDs[16] or uni-polar devices[15] is related to (i) treating these systems as 1D as well as (ii) the semi-classical nature of DD models. Regarding (i), theoretical and experimental studies have revealed that the electronic and optical properties of III-N-based heterostructures are strongly affected by alloy fluctuations and accompanying carrier localization,[17,18] all of which is not fully reflected within a 1D DD transport model.[15,16,19] Furthermore, (ii) the semi-classical nature of DD models neglects quantum mechanical effects, such as tunneling. Fortunately, such quantum effects can be included, to some extent, in DD simulations via the so-called localization landscape theory (LLT)[20–22] or the (nonlocal) effective potential method to smooth band edges.[23–25]

Thus, to accurately guide the design of future III-N-based LEDs, a fully three-dimensional (3D), ideally atomistic, transport model that includes quantum mechanical effects for the *entire* device is required. While atomistic calculations have been performed to target these questions,[26,27] such a treatment is numerically extremely expensive.[16] This becomes even more challenging when device performance studies are required, where, for instance, the well width or the composition in the well and barrier regions of the device is systematically modified. Given the numerical burden of the fully atomistic and quantum mechanical solvers, the workhorse for transport calculations still remains largely DD. The challenge here is now to transfer atomistic effects accurately into a modified, quantum-corrected DD transport model. Previous work, targeting, for instance, (In,Ga)N LED or uni-polar devices, tackled such a multiscale problem in the following way:[16,28] First, a random distribution of In and Ga atoms on either a cubic or wurtzite grid is generated. Second, based on such a distribution, the local In content is determined by using averaging procedures on the underlying grid. Equipped with this information, continuum-based strain and built-in field calculations are performed, which can then be used to generate an "energy landscape" (conduction and valence band edges/confining potential), mainly in the framework of a single-band effective mass approximation (EMA). This information can either be directly used for 3D DD-based transport calculations or even coupled with LLT to account for quantum corrections. It is important to note that such an approach relies on (i) identifying an interpolation procedure for the local alloy content, (ii) the knowledge of how related material parameters change with composition locally, and (iii) assuming that bulk parameters can be used locally to obtain strain and built-in field effects. Finally, it assumes that even when including random alloy fluctuations, the modified continuum-based single-band EMA describes the electronic structure of this complicated system accurately. Thus, overall "atomistic" aspects enter mainly at the In atom distribution level. However, it is difficult to judge how well local fluctuations in strain or built-in fields are captured in comparison with a fully atomistic approach (valence force field plus local polarization theory). Furthermore, consequences of alloy fluctuations for the electronic structure of the well and again how this compares to a fully atomistic description, e.g., tight-binding, are not widely discussed or analyzed.

We have recently established a theoretical framework that allows one to target these questions,[29] which works as follows: First, we generate an energy landscape that is directly obtained from an atomistic tight-binding (TB) model, which accounts for random alloy fluctuations and connected fluctuations in strain and built-in fields on a microscopic level. Second, the electronic structure of, e.g., an (In,Ga)N QW, can be calculated within TB and a single-band EMA (using this landscape) so that the data can be directly compared since both operate on the same alloy microstructure. Here, in principle, the only free parameter in the modified EMA is the effective mass; the confining potential (band edges) is directly obtained from the TB model. Our results showed that when operating on the same alloy microstructure (alloy configuration) and the same confining energy landscape, the modified EMA significantly overestimates the bandgap/transition energy of (In,Ga)N/GaN QWs, at least for In contents larger than 5%. However, as the calculations were performed on the same alloy microstructure, it allows one to adjust the EMA. We have found that using a rigid energy shift within the QW region results in a good agreement between TB and EMA, at least in terms of transition energies and the distribution of (localized) energy states.[29]

In this work, we extend the theoretical framework above to study charge carrier transport in III-N-based devices. We give the details of the method and apply it to uni-polar transport in single QW (SQW) and MQW (In,Ga)N systems. In general, we use the energy landscape calculated from our atomistic TB model in conjunction with LLT to generate a quantum-corrected energy landscape. This landscape presents the backbone of our DD simulation. For the active (In,Ga)N QW region, we use a finite-element mesh with as many nodes as atomic lattice sites, which we later enlarge to work in combination with a specialized finite volume method. In doing so, (*n*-doped) contact regions can be added to the system on a much coarser grid to model a full device. We highlight that the developed approach can be extended to investigate complete (In,Ga)N-based LED structures (*p*–*i*–*n* systems) as well as AlGaN-based UV LEDs in future studies.

Our obtained results for uni-polar (In,Ga)N SQW and MQW structures show that when including LLT and alloy fluctuations, smaller turn-on voltages are observed in comparison with a standard virtual crystal approximation (VCA) calculation; this agrees with previous studies.[15,16] Furthermore, and as discussed already above, "standard" 1D uni-polar electron transport calculations, which effectively correspond to our VCA results, give too large turn-on voltages when compared to experiment. The fact that our full 3D model gives smaller turn-on voltages compared to VCA suggests already an improved description of experimental findings and highlights again the importance of quantum corrections and alloy fluctuations for an accurate description carrier transport in (In,Ga)N-based devices. We stress that our results are achieved without any re-fitting/adjusting of, e.g., piezoelectric coefficients,

which is often applied in "conventional" 1D DD calculations found in the literature.[30,31]

The remainder of the paper is organized as follows: We present the theoretical ingredients of our multiscale model, namely, TB, LLT, and DD, as well as the mesh generation (additional information is supplied in an Appendix) in Sec. II. Our results for unipolar transport in (In,Ga)N-based SQW and MQW systems are detailed in Sec. III. Finally, we summarize our framework and the results in Sec. IV.

II. THEORETICAL FRAMEWORK: FROM AN ATOMISTIC ENERGY LANDSCAPE TO DRIFT–DIFFUSION SIMULATIONS

We present and discuss the different ingredients of our multiscale framework in this section. We start in Sec. II A with the TB model and briefly describe the procedure to generate an energy landscape that contains the contributions from random alloy fluctuations and thus associated strain and built-in field fluctuations. Section II B details how the obtained landscape is transferred to a finite-element method (FEM) mesh, which presents the starting point for our charge carrier transport calculations. Utilizing this mesh, Sec. II B gives details on (i) how the random alloy fluctuations are treated for later transport calculations and (ii) how the LLT equation is solved on the underlying FEM mesh. The uni-polar transport model based on the derived energy landscape, which we employ for our numerical studies, is introduced in Sec. II D; here, we also describe how the spatially varying band edges are handled numerically.

A. Tight-binding model and local band-edge calculations

In order to capture the effects of (random) alloy fluctuations on the conduction (CBE) and valence band edges (VBE) and ultimately on the electronic structure of the QW active region of a III-N device, we employ atomistic TB theory. In the following, we give a brief overview of the underlying model and how to extract local band edges from a TB model; more details can be found in Refs. 17, 29, and 32. While this approach is general, we discuss in the following an (In,Ga)N/GaN QW system as an example.

The backbone of our theoretical framework is an empirical nearest neighbor sp^3 TB model.[32] The TB parameters were determined by fitting GaN and InN bulk TB band structures to the corresponding hybrid functional density functional theory (DFT) band structures.[32] Given the (large) lattice mismatch between InN and GaN (≈10%), strain effects have to be taken into account in (In,Ga)N/GaN QWs. To obtain an atomistic resolution of the strain in such a structure, the equilibrium positions of all the atoms in the simulation supercell are obtained using a valence force field (VFF) model,[17,32] which has been implemented in the software package LAMMPS.[33] As already discussed above, III-N heterostructures in general exhibit built-in (spontaneous and piezoelectric) polarization vector fields. To account for (local) polarization effects in (In,Ga)N/GaN QWs, a local polarization theory[32] is employed. The TB model summarized in this paragraph has been extensively benchmarked against DFT as well as experimental data.[32,34]

As highlighted above, a key ingredient for DD transport calculations is the (local) CBE and VBE. This information can now be extracted from our TB model by diagonalizing the Hamiltonian at each lattice site.[29] Our previous work[29] already revealed that when using this atomistically generated landscape directly in conjunction with an effective mass model, electron as well as hole ground state energies, and thus the connected transition energies, are significantly underestimated, at least for systems with In contents larger than 5%. However, the broadening of the energy spectrum due to alloy fluctuations was in good agreement between the models, even though carrier localization effects may not be treated accurately in the EMA. The overall agreement between TB and EMA can be improved in terms of transition energies, energy spectrum broadening, and to some extent carrier localization characteristics by applying a (composition dependent) rigid shift to the band edges in the QW region. We apply this approach here too. In doing so, we find indeed good agreement between TB and results obtained within LLT when operating on the confining potential landscape extracted from TB.

B. Device mesh generation for transport calculations

The obtained local band edges on the atomistic wurtzite lattice sites need to be transferred to a mesh that allows us to perform the transport calculations. Two aspects are important here. First, the mesh needs to be fine enough to capture alloy fluctuations in the active region. Second, in regions where no alloy fluctuations are present, the band-edge energies can be obtained from the literature (e.g., *n*-doped GaN contacts). In this contact region, the mesh can also be chosen much coarser when compared to the atomistic region; this helps to keep the computational cost low. The latter part is very important to make self-consistent 3D DD simulations feasible. A schematic illustration of our approach to address this challenge is shown in Fig. 1. We start from an atomistic TB energy landscape as discussed above and ultimately construct a larger mesh for the DD simulations.

Next, we discuss the post-processing within the atomistic region before we explain the embedding into the larger mesh. Using the atom lattice sites as nodes, we construct a FEM mesh via TetGen.[35,36] The TB energy landscape determines the energy values at the nodes. We stress again that the underlying TB mesh with In, Ga, and N atoms is not used to generate a composition profile/map on which local averages for continuum-based calculations are determined; we use TB directly to define the energy landscape. Figure 2(a) depicts the TB model data for a 3.1 nm thick $In_{0.1}Ga_{0.9}N$ SQW in the x–z-plane, where the z-axis is parallel to the wurtzite c-axis. The depicted test structure has 38 150 atoms and the corresponding FEM mesh has 38 150 nodes, and 280 816 tetrahedra [see Fig. 2(b)]; this mesh represents the atomistic region discussed above. We have employed this transfer of TB data to an atomistic FEM mesh previously[29] to compare the electronic structure of (In,Ga)N/GaN QWs when using atomistic and continuum methods.

In order to perform full-device calculations, contact regions (e.g., n-doped GaN contacts) have to be attached to the atomistic region of the simulation. In the context of DD simulations for semiconductor devices, the finite-volume method (FVM) has been exceptionally successful. Our specific approach described in detail in the Appendix requires a mesh that ensures that the numerical

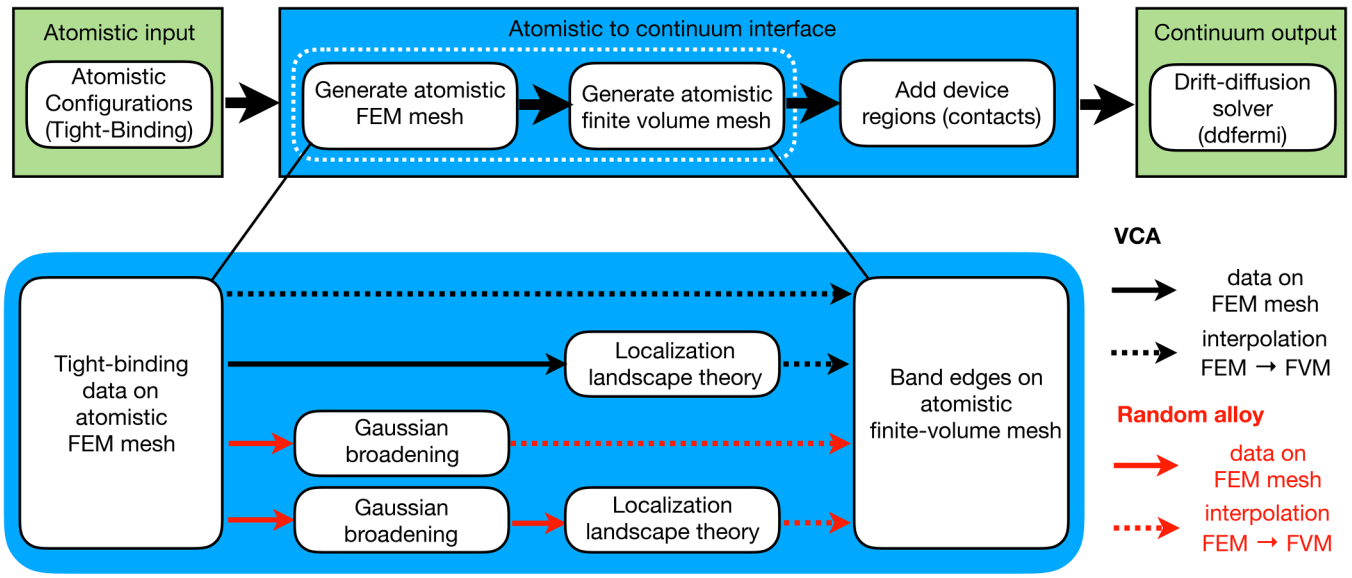

FIG. 1. Schematic workflow to connect an atomistic tight-binding model to a continuum-based drift–diffusion solver (here ddfermi). The connection between the atomistic and continuum-based grid is achieved in three steps. First, we generate an atomistic finite-element method (FEM) mesh with as many nodes as atomic sites. The data on the FEM mesh are then interpolated on a Voronoi finite-volume method (FVM) mesh needed for stable drift–diffusion simulations. Finally, the FVM mesh is enlarged by adding coarser contact and intrinsic regions. The inset details four different ways atomistic band-edge data are transferred to the FVM mesh. Whereas the data paths indicated in black refer to the VCA type of data, the data paths in red refer to random alloy data. Solid arrows indicate an operation (stated in the box) on the FEM mesh, and dashed arrows indicate interpolation to the FVM mesh. The meshes are shown visually in Fig. 2.

fluxes are perpendicular to the cell interfaces. Such a mesh is dual to a boundary conforming a Delaunay tetrahedral mesh. Therefore, the next step is the generation of such a finite-volume mesh from the atomistic FEM mesh, which satisfies this additional requirement. Again via TetGen, we produce a so-called boundary-conforming Delaunay tetrahedral mesh (for details, see the Appendix), which includes the original FEM lattice sites and interpolate the atomistic data onto it; see Figs. 2(b) and 2(c). The FVM mesh has 47 248 nodes and 305 272 tetrahedra. Finally, we attach coarser intrinsic meshes as well as n-doped GaN contact regions to both sides of the atomistic region, again using TetGen. Thus, a complete n–i–n diode has been created, see Fig. 2(d), which contains the atomistic region (box with yellow-dashed lines), the coarse grained intrinsic GaN (light blue and green), and n-doped GaN (red and purple) regions. While as a test system we have used here an n–i–n structure, the approach can now be easily adapted for a p–i–n setup or other material systems. The resulting boundary-conforming finite-volume mesh of the complete n–i–n structure has in total 61 202 nodes and 369 430 tetrahedra and can be used for DD simulations with ddfermi.[37] The tool chain for creating the combined meshes and transferring TB data has been implemented with WIAS-pdelib[38] and TetGen.[35,36]

C. Localization landscape theory and random alloy fluctuations on a FEM mesh

Having transferred the TB band-edge data to a larger mesh with contact regions as described above, care must be taken when performing DD simulations on this mesh. It has already been discussed in the literature that for transport properties, the spatial length scale of the potential fluctuations is effectively determined by the de Broglie wavelength.[16] Consequently, charge carrier wave functions sample a wider "area" of the confining energy landscape rather than just a single lattice site. While in VCA this may be of secondary importance, in a strongly fluctuating energy landscape, it is important to account for this. The question has been discussed in detail in Ref. 16, and the authors applied a Gaussian averaging procedure to determine the local alloy content. The same *ad hoc* procedure has been employed by DiVito *et al.*[28] While we follow a similar approach here and employ Gaussian averaging, we employ this to the original *band-edge profile* E_c^{TB} from TB

$$E_c^{\sigma}(\mathbf{x}_i) = \frac{\sum_j E_c^{\mathrm{TB}}(\mathbf{x}_j)\exp\left(-\frac{(|\mathbf{x}_i-\mathbf{x}_j|)^2}{2\sigma^2}\right)}{\sum_j \exp\left(-\frac{(|\mathbf{x}_i-\mathbf{x}_j|)^2}{2\sigma^2}\right)} \tag{1}$$

but *not* to the alloy content. Here, $E_c^{\sigma}(\mathbf{x}_i)$ is the CBE energy at the (lattice) site $\mathbf{x}_i$; σ denotes the Gaussian width and acts as a smoothing parameter. This averaging procedure is of course only relevant within the QW(s) and near the well–barrier interface. This scheme has been implemented for the FEM mesh. Nodal values will be interpolated to a finer boundary conforming the FVM mesh, following the approach described in Sec. II B. Given that we will focus our attention on uni-polar transport, this procedure will be applied to the CBE but can in future studies also be applied to the VBE.

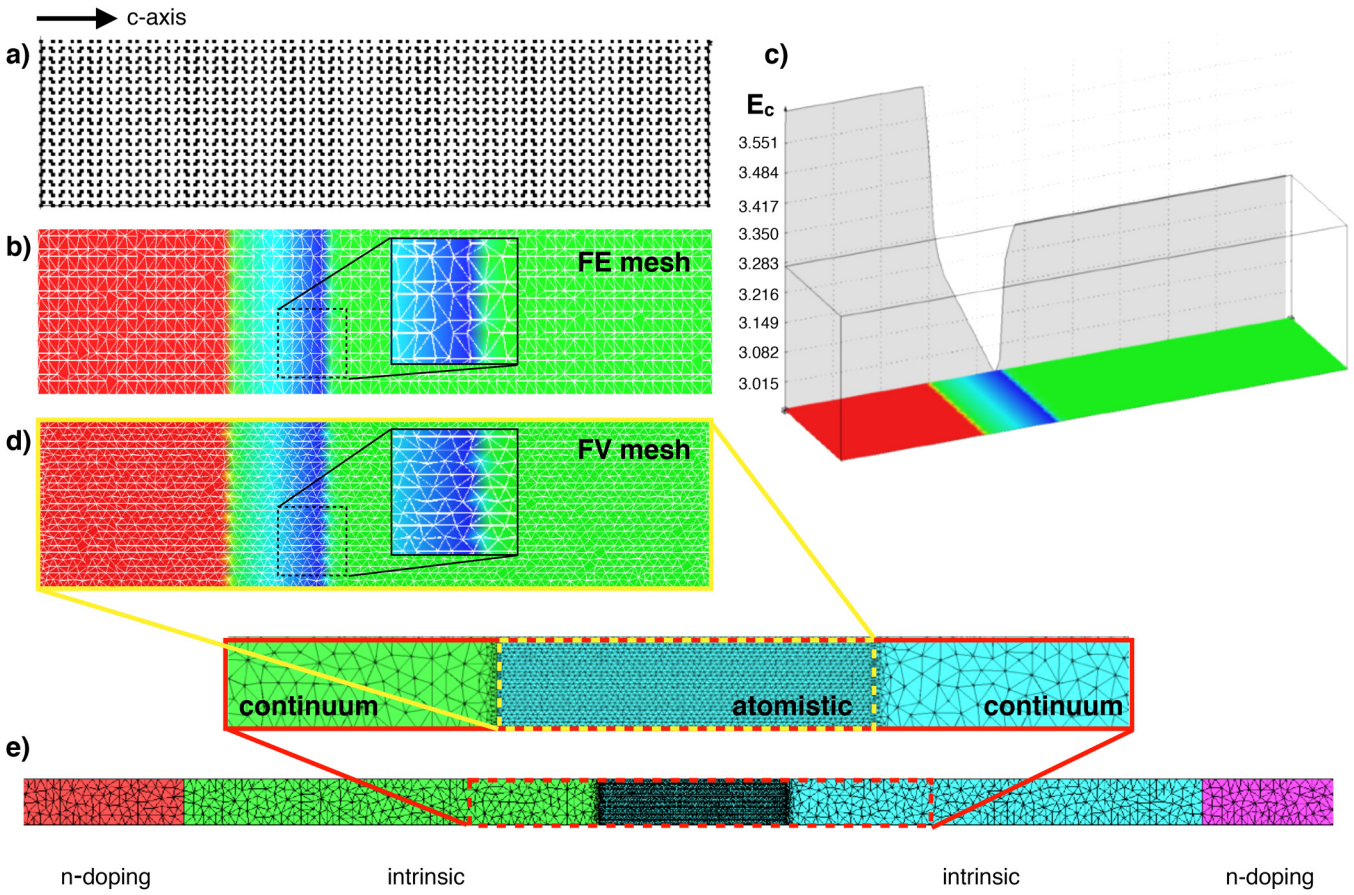

FIG. 2. Transfer of atomistic data to a larger finite-volume mesh for continuum-based drift–diffusion simulations. We start with a point set (a) defined by the atomistic lattice sites as provided by tight-binding. Using TetGen, a tetrahedral finite-element mesh (b) is generated, which has exactly the same number of nodes as there are atoms in (a). In doing so, the tight-binding input is exactly represented on the nodes of the atomistic finite-element method mesh. The colors in (b) represent the values of the conduction band edge E_c, and (c) depicts the E_c profile of an $In_{0.1}Ga_{0.9}N$ single quantum well in virtual crystal approximation. The data from the atomistic finite-element method mesh are then interpolated to a finite-volume mesh (d), namely, a boundary-conforming Delaunay triangulation generated by TetGen.[35,36] After attaching intrinsic device regions and doped contact regions to the atomistic region, the full 3D device mesh (e) for drift–diffusion simulations is established.

We stress again that in Refs. 16 and 28 the In content at each point is computed from a Gaussian average, and then the strain, built-in field, and ultimately the CBE are evaluated in a pure continuum framework. We go beyond this by calculating the CBE (the confining potential) at each (lattice) site from the atomistic TB approach, with no need to calculate local strain or built-in potentials in a continuum-based framework before applying a Gaussian function to the confining potential. Thus, in comparison with Refs. 16 and 28, we have here *a posteriori* broadening and transfer the atomistic effects on the band offset, strain, and built-in field due to alloy fluctuations directly into the confining energy landscape before averaging.

In general, employing such a Gaussian averaging procedure comes at the cost of having to correctly determine the width, σ, *a priori*. To analyze the impact of the σ on the CBE profile, which ultimately will also impact the transport, Fig. 3 shows the profile of $E_c^\sigma - q\psi$ in a 3.1 nm wide $In_{0.1}GaN_{0.9}/GaN$ SQW, comparing random alloy fluctuations with different Gaussian widths σ to a VCA. Here, ψ denotes the electrostatic potential in the n–i–n device, including also piezoelectric and spontaneous polarization effects; q denotes the elementary charge. At each plane along the c-direction, the full range of CBE values over the x–y plane is shown, which allows clear visualization of the impact of the alloy fluctuations on the CBE. Several features are important. The most striking difference between the VCA and the smoothed random alloy (RA) CBE is that the potential barrier between the GaN and (In,Ga)N QW material is significantly reduced. This feature is expected to reduce the turn-on voltage of the device and will be discussed in detail further below. Moreover, the barrier–well interface reduces further with increasing σ. However, the reduction between $\sigma = 0.6$ nm and $\sigma = 0.9$ nm is smaller than the reduction from $\sigma = 0.3$ nm to $\sigma = 0.6$ nm, even though the difference in σ values is

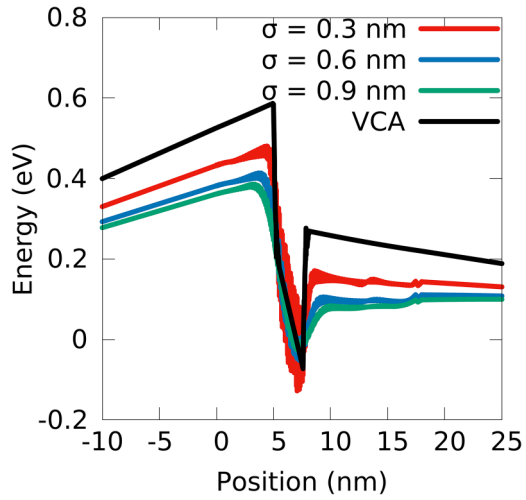

FIG. 3. Randomly fluctuating, smoothed conduction band-edge profile along the *z*- (*c*)-axis of an *n*–*i*–*n* $In_{0.1}Ga_{0.9}N$/GaN single quantum system at zero bias (more details given in the main text). The results are displayed in the *absence* of quantum corrections via LLT but for three different Gaussian widths σ, namely, $\sigma = 0.3$ nm (red), $\sigma = 0.6$ nm (blue), and $\sigma = 0.9$ nm (green), as well as for a "standard" virtual crystal approximation (VCA, black).

the same ($\Delta\sigma = 0.3$ nm). We also note that while the average band-edge energy in the well is basically unaffected by different σ values, the CBE fluctuations in the well noticeably reduce. Consequences of these effects on the current–voltage characteristics are discussed below.

Having determined the local band edges from atomistic TB theory, we can now also include quantum corrections using LLT.[21] These corrections are not limited to a calculation that accounts for random alloy fluctuations; LLT can also be used in conjunction with a VCA description. We note that many commercial software packages targeting carrier transport properties of III-N devices also have the option to include quantum mechanical effects by solving Schrödinger's equation in the active region (QW region) of a device. However, such an approach is numerically very demanding even for a 1D simulation, not to mention a full 3D calculation, which is necessary in the presence of random fluctuations. When using LLT, one avoids having to solve the Schrödinger equation and thus a large eigenvalue problem. In LLT, one is left with a linear partial differential equation, given by[21]

$$\hat{H}^{\mathrm{EMA}} u := -\frac{\hbar^2}{2m^*}\Delta u + Vu = 1. \tag{2}$$

Here, $\hat{H}^{\mathrm{EMA}}$ denotes a single-band effective mass Hamiltonian, m^* the effective (electron or hole) mass, and V the confining potential energy. For the confining potential, V, we use our TB band-edge data. Here, VCA data, $V = E_c^{\mathrm{VCA}}$, or random alloy data, $V = E_c^{\sigma}$, for different σ values can be used. As described in detail in Refs. 16 and 21, once u is determined by solving Eq. (2) with appropriate boundary conditions, one can also extract an effective confining potential W via

$$W(\mathbf{x}_i) = 1/u(\mathbf{x}_i). \tag{3}$$

This effective potential for the energy landscape can be used in DD simulations to include both random alloy fluctuations and quantum corrections at the macroscopic DD scale.[16] More details on LLT are found in Refs. 16, 21, and 22.

Regarding the computational aspects, we numerically solve the LLT equation, Eq. (2), supplied with appropriate Dirichlet and Neumann boundary conditions on the atomistic FEM mesh via a standard FEM.[39] The Dirichlet conditions are applied on the left and right boundaries of the atomistic FEM mesh shown in Fig. 2(b) and are implemented via a penalty technique.[40] The FEM discretization is implemented in WIAS-pdelib,[38] using PARDISO as a linear solver.[41]

Since LLT basically replaces the Schrödinger equation, LLT provides also information about the energy spectrum and the wave functions.[42] Thus, the outcome of the LLT calculations can be directly compared to our TB data. For the SQW structures analyzed in Sec. III, we find very good agreement between TB and LLT when applying a rigid band-edge shift of 129 meV and in line with Ref. 29. All of these provides a feedback loop between our atomistic model, the obtained landscape, and the resulting electronic structure. This benchmarking gives further confidence that the here established simulation framework for performing transport calculations captures alloy fluctuations accurately in SQWs.

Examples for the resulting effective energy landscapes/confining potential energies $W - q\psi$ are given in Fig. 4. We observe that similar to the random alloy case *without* quantum corrections, cf.

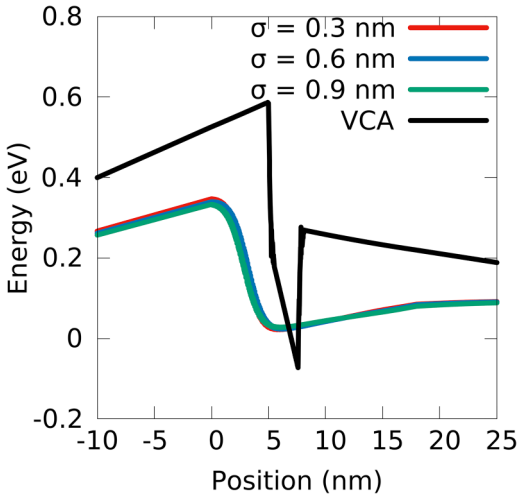

FIG. 4. Randomly fluctuating, smoothed conduction band-edge profile along the *z*- (*c*)-axis of an *n*–*i*–*n* $In_{0.1}Ga_{0.9}N$/GaN single quantum well system at zero bias (more details given in the main text). The results are displayed in the *presence* of quantum corrections via LLT but for three different Gaussian widths σ, namely, $\sigma = 0.3$ nm (red), $\sigma = 0.6$ nm (blue), and $\sigma = 0.9$ nm (green), as well as a "standard" virtual crystal approximation (VCA, black).

Fig. 3, the LLT treatment leads also to a reduction in the potential barrier between the GaN material and (In,Ga)N QW. Therefore, the strongly fluctuating TB landscape is "softened," given that the carrier wave functions sample a wider "area" on this landscape, as one may expect from a quantum mechanical wave function analysis. However, two additional aspects are important to note. As already highlighted above, LLT can not only be combined with the random alloy system, but can also be employed in a VCA type calculation. Thus, from a VCA plus LLT description, it is also expected that the potential barrier between the GaN and the (In,Ga)N QW material is reduced. Therefore, including quantum corrections in VCA should also affect the turn-on voltage of a device when compared to a "standard" VCA calculation without quantum corrections. Second, as one can infer from Fig. 4, once LLT has been applied, increasing the Gaussian width σ for the CBE softening in the random alloy case has very little impact on the resulting band-edge profile. Below, we will analyze this aspect in greater detail when looking at the I–V curves of (In,Ga)N/GaN-based uni-polar devices.

D. Uni-polar drift-diffusion model with spatially varying band edges

In Secs. II A–II C, we have discussed the mesh generation and also how random alloy fluctuations and quantum corrections in the confining potential are treated. In this section, we focus our attention on the semi-classical van Roosbroeck system, which models DD charge transport in semiconductors.[43] As discussed above, we simulate here uni-polar DD transport in (In,Ga)N-based systems. However, the framework is general and can be directly transferred to the bipolar case.

For a bounded spatial domain $\Omega \subset \mathbb{R}^d$ where $d \in \{1, 2, 3\}$, the stationary van Roosbroeck system[44] consists of two coupled nonlinear partial differential equations of the form

$$-\nabla \cdot (\varepsilon_s(\mathbf{x})\nabla\psi(\mathbf{x})) = q(C(x) - n(x)), \tag{4a}$$

$$\nabla \cdot \mathbf{j}_n = 0 \tag{4b}$$

for $\mathbf{x} \in \Omega$. The Poisson equation, Eq. (4a), describes the electric field $\mathbf{E} = -\nabla\psi$ that is generated by a scalar electric potential $\psi(\mathbf{x})$ in the presence of a free charge carrier density. Here, $\varepsilon_s(\mathbf{x}) = \varepsilon_0\varepsilon_r(\mathbf{x})$ describes the position dependent dielectric constant and q is the elementary charge. In a (doped) uni-polar semiconductor device, the charge density is given by the density of free (negatively charged) conduction band electrons, $n(\mathbf{x})$, and the density of ionized built-in dopants, $C(\mathbf{x}) = N_D^+(\mathbf{x})$, where N_D^+ denotes the density of singly ionized donor atoms. The current density $\mathbf{j}_n(\mathbf{x})$ is given by the usual expression[43]

$$\mathbf{j}_n(\mathbf{x}) = -q\mu_n n(\mathbf{x})\nabla\varphi_n(\mathbf{x}). \tag{5}$$

That is, the negative gradient of the quasi Fermi potential, $\varphi_n(\mathbf{x})$, is the driving force of the current; $\mu_n(\mathbf{x})$ denotes the free carrier mobility.

Using the Boltzmann approximation, the densities of free carriers, $n(\mathbf{x})$, in a solid are given by

$$n(\mathbf{x}) = N_c \exp\left(\frac{q(\psi(\mathbf{x}) - \varphi_n(\mathbf{x})) - E_c^{dd}(\mathbf{x})}{k_B T}\right), \tag{6}$$

where k_B is the Boltzmann constant, T denotes the temperature, $E_c^{dd}(\mathbf{x})$ is the (position dependent) band-edge energy used in the transport calculations, and N_c is the effective density of states,

$$N_c = 2\left(\frac{2\pi m_e^* k_B T}{\hbar^2}\right)^{3/2}.$$

We note that we have different options for setting the band-edge energy E_c^{dd} in the DD simulations. One may choose (smoothed) TB data $E_c^{dd} = E_c^{\sigma}$, VCA results $E_c^{dd} = E_c^{\mathrm{VCA}}$, or the outcome of LLT calculations $E_c^{dd} = W$. A schematic illustration of the different options is given in the inset of Fig. 1. Equation (6) indicates that the electric potential, ψ, leads to a bending of the energy landscape, $E_c - q\psi$, and thus results in a nonlinear, self-consistent coupling to the carrier densities. In the following, we assume a globally constant temperature for carriers and the crystal lattice of $T = 300$ K.

We note that, for instance, due to random alloy fluctuations, the CBE E_c varies spatially. Thus, the electron flux, Eq. (5), needs to be correctly discretized. To this end, we extend the well-known local Scharfetter–Gummel flux approximation[47] to variable band edges, here shown for the CBE E_c. Since by construction of the FVM mesh (more details in the Appendix), the cell edges are orthogonal to the fluxes, and we may consider only 1D fluxes,

$$j_n = -z_n q\mu_n U_T N_c \frac{1}{h}\left\{B\left(-z\frac{\delta\psi - \delta E_c/q}{U_T}\right)\exp(\eta_{n,L}) - B\left(z\frac{\delta\psi - \delta E_c/q}{U_T}\right)\exp(\eta_{n,K})\right\}. \tag{7}$$

The parameter $z_n = -1$ is the charge number for electrons, $B(x) = x/(\exp(x) - 1)$ denotes the Bernoulli function, $U_T = \frac{k_B T}{q}$ the thermal voltage, $\delta\psi = \psi_L - \psi_K$, $\delta E_c = E_{c,L} - E_{c,K}$, and

$$\eta_{n,P} = z_n \frac{E_{c,P} - q(\psi_P - \varphi_{n,P})}{k_B T}, \quad P \in \{K, L\}.$$

The subindices K and L refer to the nodes $\mathbf{x}_K$ and $\mathbf{x}_L$ associated with the corresponding cells. Further details of the numerical implementation of the above expressions, especially how to embed all this into a finite-volume framework, are given in the Appendix. The physical parameters used in the DD simulations are listed in Table I.

III. RESULTS

In this section, we apply the developed framework to uni-polar, n-doped/intrinsic/n-doped (n-i-n), (In,Ga)N/GaN-based devices: We analyze the impact of random alloy fluctuations and quantum corrections introduced by LLT on the I–V curves of such

TABLE I. Material parameters used in drift–diffusion simulations. Unless otherwise stated, all parameters are taken from Ref. 16.

Physical quantity	Value	Units
m_e^* GaN	0.2	m_0
m_e^* InN	0.07	m_0
μ_n *n*-GaN	200	$cm^2/(V\ s)$
μ_n *i*-GaN	440[45]	$cm^2/(V\ s)$
μ_n *i*-(In,Ga)N	300	$cm^2/(V\ s)$
ε_r^{GaN}	9.7[46]	ε_0
ε_r^{InN}	15.3[46]	ε_0

structures. The results are compared with the data obtained from a VCA description of the same structures. Special attention is paid to the impact of the Gaussian broadening width, σ, on the results. This analysis is carried out for both SQW systems, Sec. III A, as well as for MQW structures consisting of three wells, Sec III B. For all these calculations, the well width is 3.1 nm, the In content in the well is 10%, and the barrier material is GaN. In the MQW system, the width of the barrier between the wells is 8.0 nm. Figure 5 gives a schematic illustration of the system. Except for the VCA systems, all calculations make a random alloy assumption for the InGaN alloy forming the QW; any additional penetration of In atoms into the GaN barrier is not considered. The assumption of such an abrupt interface between InGaN and GaN is consistent with the experimental data in Ref. 18, at least for growth of InGaN on GaN. When capping an InGaN QW with GaN, penetration of In atoms into the GaN barrier may occur. However, recent experimental studies show that by a careful choice of the growth conditions, this effect can be reduced.[48] Given that we are interested in establishing a general simulation framework, these In atom "bleeding" effects are of secondary importance for the present study but can be incorporated in future investigations.

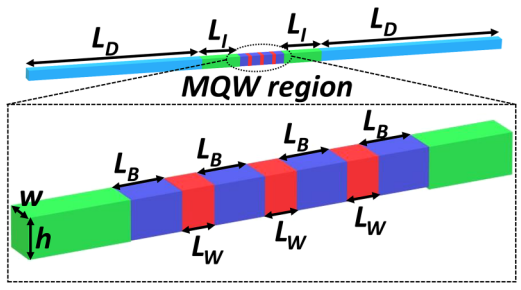

FIG. 5. Schematic illustration of the simulation cell with three quantum wells (QWs) in the active region. The *n*-doped regions (light blue) have a doping density of $n = 5 \times 10^{18}\ cm^{-3}$ and a length of $L_D = 160$ nm. The intrinsic regions on the coarse mesh (green) have a length of $L_I = 40$ nm. The atomistic region, also assumed as intrinsic, contains regions of a GaN barrier material (dark blue) with a length of $L_B = 8.0$ nm and $In_{0.1}Ga_{0.9}N$ QWs (red) with a length of $L_W = 3.1$ nm. The simulation cell has an in-plane dimension of $w \times h = 5.1 \times 4.4\ nm^2$ along the entire system.

A. (In,Ga)N SQW system

In the first step and before looking at a full current–voltage (I–V) curve of the $In_{0.1}Ga_{0.9}N$ SQW system, we focus our attention on the impact of random alloy fluctuations on the results. More specifically, we will study the impact of the Gaussian width σ and thus the related smoothing of the energy landscape on the current. Figure 6 displays the current in the system at a fixed bias of 3V for different σ values. The data are shown when including and when neglecting quantum corrections arising from LLT. The calculations have been performed for five different random alloy configurations in the QW, allowing us to also study the influence of the alloy microstructure on the current; the error bars indicate the standard deviation. One can infer from Fig. 6 that when neglecting LLT effects, the resulting current (strongly) depends on the width of the Gaussian function, at least for $\sigma < 0.6$ nm ($\approx 2a$, where a is the in-plane lattice constant of GaN). Above this threshold, the dependence of the current I on σ is less pronounced. We will discuss the impact of σ on the full I–V curve further below, but noting here that σ may impact the results. In the literature, the value of σ has, for instance, been estimated using atom probe tomography data, and a value of $\sigma_{APT} = 0.6$ nm has been assumed.[16] Turning now to the calculations including quantum corrections via LLT, Fig. 6 reveals that once these effects are taken into account, σ is of secondary importance for the obtained current I at the fixed bias of 3V; this is at least the case for a SQW. We note, however, that this aspect may depend on the in-plane dimensions of the simulation cell and thus needs to be carefully investigated when performing calculations that include random alloy fluctuations in general. This observation agrees with our earlier conclusion that Gaussian smoothing does not affect the band-edge profile, see Fig. 4, when including LLT effects in the calculations.

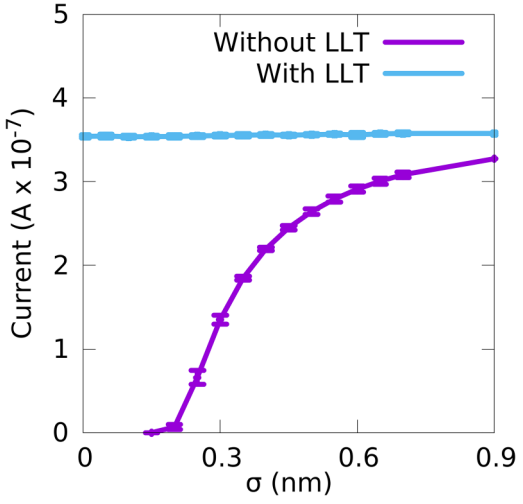

FIG. 6. Current I at a bias of 3V as a function of the Gaussian width, σ, without LLT (purple) and with LLT (blue) corrections for an *n*–*i*–*n* system with a 3.1 nm wide $In_{0.1}Ga_{0.9}N$ single quantum well. The results are averaged over five different microscopic alloy configurations, and errors bars are given by standard deviation.

Having gained initial insight into the impact of the Gaussian width σ on the current I at a fixed voltage V, in the second step, we focus our attention now on the full I–V curve of the SQW system. Figure 7 depicts the obtained results within the different approaches. Our reference point is again a "standard" VCA (black solid line) model, which neglects both alloy fluctuations and LLT effects. In addition, we present also the data of a combined VCA and LLT treatment. Finally, Fig. 7 displays results for the random alloy case for different σ values (red lines: $\sigma = 0.3$ nm; blue lines: $\sigma = 0.6$ nm) with and without LLT effects included in the calculations. Turning to the result in the absence of LLT first, it becomes clear that when accounting for random alloy fluctuations in the model, the turn on voltage is shifted to lower values in comparison with a standard VCA description. This is also consistent with previous literature results on uni-polar transport calculations of (In, Ga)N/GaN-based QW systems.[15] However, our calculations also reveal, and in line with Fig. 6, that the obtained current at a given voltage V depends on the Gaussian width σ. As already indicated above, when neglecting quantum corrections via LLT, a further analysis is required to determine σ: if σ is too small, the resulting very strong fluctuations in the energy landscape within the well are beyond the applicability of a continuum-based DD model; if σ is too large, the fluctuations in the energy landscape are completely removed as discussed in Sec. II C. Therefore, when neglecting LLT effects, care must be taken when choosing σ.

In the second step, we turn and discuss the I–V curves when *including* effects arising from LLT (dashed lines in Fig. 7, both in the random alloy case but also in the VCA simulations). Looking at the calculations including random alloy fluctuations and LLT first, we observe that the Gaussian width σ is of secondary importance;

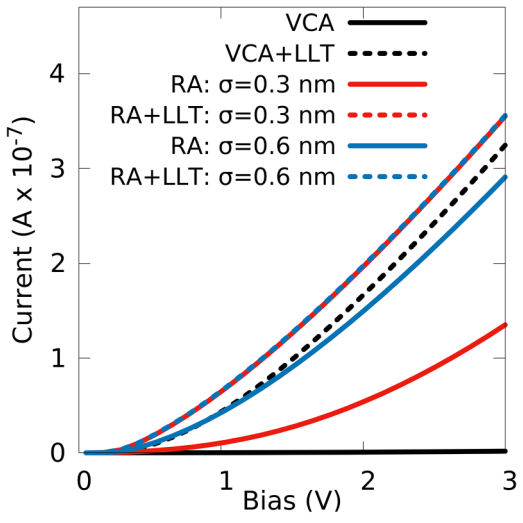

FIG. 7. Current–voltage curves for an *n–i–n* $In_{0.1}Ga_{0.9}N$ single quantum well system, within virtual crystal approximation (VCA, black) and a random alloy (RA) with Gaussian widths of $\sigma = 0.3$ nm (red) and $\sigma = 0.6$ nm (blue). Solid lines show results without quantum corrections, and dashed lines denote results with quantum corrections included via localization landscape theory.

this is again consistent with our findings in Figs. 4 and 6. We note also that when choosing a relatively large value of σ (e.g., 0.6 nm), the random alloy I–V curves with and without LLT (blue) do not differ significantly. We attribute this to the effect that both LLT and a relatively large Gaussian broadening soften the well–barrier interface and thus reduce the resistivity of the system. Furthermore, the fluctuations in the energy landscape within the QW are reduced, leading to a further decrease in the resistance of the QW region. We note that in the presented test system, the in-plane dimensions of the simulation cell are relatively small, and further test on the impact of σ on the I–V curve may be required in future studies. However, this is beyond the scope of the present work, which introduces the general framework. Nevertheless, our results show that the calculations including random alloy fluctuations and LLT effects give the lowest turn-on voltage and highest current compared to all other models discussed here. However, and interestingly, we find also that the VCA plus LLT calculations give almost the same I–V curve as the quantum-corrected random alloy simulations. This indicates that for a SQW, once LLT is included in the model, the VCA can provide a very good approximation of the I–V characteristics of the uni-polar *n–i–n* system in comparison with a full 3D random alloy model. Furthermore, since the (3D) VCA neglects any in-plane variation in the system, already, a 1D VCA simulation seems to lead to reliable results—as long as LLT is included. Having only to rely on a 1D simulation would obviously reduce the computational cost immensely compared to a full 3D calculation including alloy fluctuations. However, and as we will show in Sec. III B, for a MQW system, a 1D VCA plus LLT calculation is no longer sufficient.

B. (In,Ga)N MQW system

Having discussed a SQW system in Sec. III A, we focus our attention now on a MQW system. Figure 8 shows the I–V curves for a MQW system consisting of three $In_{0.1}Ga_{0.9}N$/GaN QWs with a barrier width of $L_B = 8.0$ nm. Here, we followed the approach of the SQW, and calculations have been performed using either a VCA treatment or account for random alloy fluctuations in the system. Again, the simulations are carried out both with and without quantum corrections via LLT.

As in the SQW case, VCA calculations neglecting LLT effects show the highest turn-on voltage and lowest current when compared with all other data. When combining VCA and LLT, we find similar to the SQW case that the turn-on voltage is reduced and the current density is increased. However, and this is in *strong contrast* to the SQW data, cf. Fig. 7, in the MQW system, the results from VCA plus LLT deviate noticeably from the outcome of calculations that accounted for both random alloy fluctuations and LLT; cf. Fig. 8. We also note that VCA plus LLT simulations show significant deviations (lower currents, higher turn-on voltages) from random alloy calculations that neglect LLT effects. Overall, we attribute the aspect that random alloy fluctuations seem to become more important in the MQW system to inherent features of LLT. As discussed, for instance, in detail in Refs. 21 and 22, to predict the ground state energy of a QW uainf LLT, the so-called reference energy, E_{ref}, has to be chosen appropriately. However, the choice of E_{ref} not only affects the prediction of the ground state energy of the

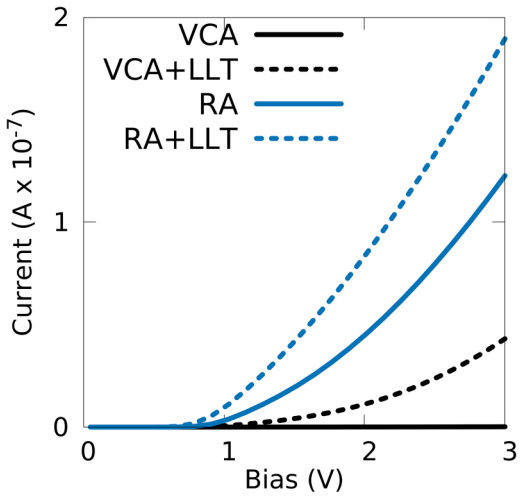

FIG. 8. Current–voltage curves for a three $In_{0.1}Ga_{0.9}N$ quantum well system, within virtual crystal approximation (VCA, black) and when random alloy (RA) fluctuations (Gaussian width of $\sigma = 0.6$ nm) are included in the model (blue). Solid lines indicate results without quantum corrections, and dashed lines show results with quantum corrections included via localization landscape theory.

system, but also affects the effective potential W, Eq. (2), which is used in the DD transport calculations. If the QWs in a MQW system in a DD simulation are energetically aligned, e.g., CBEs of all wells forming the MQW have approximately the same energy for an applied bias, and E_{ref} can be chosen as the bottom of the CBE. However, if there is a large difference in the CBEs of the different wells in the system, LLT may give a poorer approximation of W for the well where the CBE is energetically furthest away from the reference energy E_{ref}. When applying a bias V in an n–i–n system, this situation is often found. As a result, the softening of the well–barrier interface along with an effective decrease of the QW depth (confinement energy) may be different for the different QWs in the MQW system. Obviously, for a SQW system, this issue never arises. However, two important general aspects are to note. First, the LLT treatment of MQWs may be further improved by partitioning the MQW system into different sub-regions in which LLT is then solved separately. This means that one could calculate LLT in each region with its own reference energy and "stitch" the resulting effective potentials together. Such an advanced treatment is beyond the scope of the present work, where we are establishing a general first framework; further refinements can be made in future studies. Second, we note that in a p–i–n system, near the turn-on voltage, the QW band edges are expected to be energetically not too different. In that case, even without partitioning the system, LLT should provide a good approximation for biases near the turn-on voltage.

In principle, the same difficulties with respect to E_{ref} apply here in the random alloy systems when including LLT in the calculations. However, and compared to the outcome of VCA plus LLT studies, our results show that for simulations including alloy fluctuations but neglecting LLT, larger currents are observed. As discussed above, the calculations taking random alloy fluctuations into account automatically include some softening of the well barrier interface. Combining LLT with random alloy fluctuations results in a further increase of the current and reduction of the turn-on voltage. We stress that standard 1D VCA DD calculations presented in the literature on n–i–n (In,Ga)N QW systems always predicted much higher turn-on voltages when compared to the experimental studies.[15] Thus, the here obtained results reveal and support again the origin of this discrepancy: standard 1D VCA calculations neglect alloy fluctuations. Thus, even though E_{ref} still has to be treated carefully, the resulting energy landscape should present an improvement over VCA in terms of the predicted I–V characteristics.

While the above calculations have been performed at a fixed Gaussian width σ of $\sigma = 0.6$ nm, we still need to evaluate the impact of σ on the I–V characteristics. In the SQW case, cf. Fig. 6, the predicted current at a fixed voltage was virtually independent of σ once LLT was applied. Due to the difficulty of choosing E_{ref} in a MQW system, the current may now depend more strongly on the Gaussian width σ. However, our analysis reveals that after LLT has been applied, at a fixed voltage of 3V, the obtained currents differ only by less than 8% from the mean over a σ range from 0 to 0.9 nm (not shown). The change due to different Gaussian widths σ is only a small correction compared to the change between, e.g., VCA and random alloy fluctuation calculations, indicating again that calculations including both random alloy fluctuations and LLT are robust against changes in σ. Random alloy calculations without including LLT follow a similar trend to that of the SQW shown in Fig. 6 (purple) where the result can strongly depend on the choice of σ, particularly for σ less than 0.6 nm.

IV. CONCLUSIONS

In this work, we presented a general framework that allows us to bridge the gap between atomistic tight-binding theory and continuum-based drift–diffusion calculations. The model also includes quantum corrections via the localization landscape method to address charge carrier transport in III-N-based devices. Our approach furthermore enables a feedback loop between atomistic theory and continuum models since both operate on the same confining energy landscape. Current models in the literature mainly use modified continuum-based approaches that generate confining energy landscapes from locally averaged alloy contents and do not offer the option to compare the outcome of this with an atomistic model.

In addition to establishing and providing insight into the workflow of the overall framework, we have also targeted as a test system uni-polar electron transport in (In,Ga)N-based single and multi-quantum well structures. Overall, we find that random alloy fluctuations and quantum corrections significantly impact the current–voltage characteristics of uni-polar (In,Ga)N devices when compared to standard virtual crystal approximation studies, which are at the heart of most literature carrier transport solvers. In general and independent of single and multi-quantum well systems, the combination of quantum corrections and random alloy fluctuations leads to lower turn-on voltages and higher currents when compared to a virtual crystal approximation. Overall, this effect is very important since literature studies on uni-polar carrier transport have revealed that "standard" 1D continuum-

based transport solvers, effectively corresponding to our virtual crystal results, give turn-voltages considerably larger than the experiment. Thus, our here predicted shift to lower turn-voltages due to quantum corrections and alloy fluctuations indicates an improved description of experimental data. However, we note that the relative importance of quantum corrections and random alloy fluctuations varies between single and multi quantum well systems. We find that in the single quantum well system, quantum corrections are extremely important. As a consequence, in the single quantum well, a combined virtual crystal approximation plus LLT treatment leads to almost the same current–voltage curve as in a calculation that also includes alloy fluctuations. This indicates that for a single quantum well system, 1D calculations including LLT may be sufficient; this reduces the computational demand significantly. However, our analysis also indicates that in a MQW system this finding may not hold. In such cases alloy fluctuations are required and so a full 3D transport calculation must be carried out. Therefore, our investigations highlight that for MQW systems, both atomistic as well as quantum mechanical effects should be taken into account to achieve an accurate description of the I–V characteristics of uni-polar (In,Ga)N-based devices.

We note that while we have applied this model to uni-polar electron transport here, the toolchain is general and can thus be applied to bi-polar devices. Furthermore, it may also be employed to investigate other material systems, e.g., AlGaN, once an atomistic energy landscape is extracted. All these questions can now be targeted in future studies.

ACKNOWLEDGMENTS

The authors thank J. Fuhrmann (WIAS) for fruitful discussions. This work received funding from the Sustainable Energy Authority of Ireland and the Science Foundation Ireland (Nos. 17/CDA/4789 and 12/RC/2276 P2) and the Deutsche Forschungsgemeinschaft (DFG) under Germany's Excellence Strategy EXC2046: MATH+, project AA2-15, as well as the Leibniz competition 2020.

APPENDIX: FINITE-VOLUME DISCRETIZATION

Unlike other previous studies,[16] we discretize Eq. (4) via the finite-volume method (FVM) on Voronoi cells.[43] The 3D mesh is shown in Fig. 2(c). The construction of such a mesh from a boundary-conforming Delaunay triangulation is illustrated in Fig. 9. Here, we briefly outline our approach.

We integrate the system given by Eq. (4) over a test volume ω_k and apply Gauss's divergence theorem, resulting in the integral equations

$$-\int_{\partial\omega_k} \varepsilon_s \nabla\psi \cdot \boldsymbol{\nu}\, ds = q\int_{\omega_k} (C - n(\psi, \varphi_n))d\mathbf{x},$$

$$\int_{\partial\omega_k} \mathbf{j}_n \cdot \boldsymbol{\nu}\, ds = 0$$

for $k = 1, \ldots, N$, where N corresponds to the number of cells. Here, $\boldsymbol{\nu}$ is the outward-pointing unit normal to the control volume ω_k. These equations represent an integral form of the van Roosbroeck system discussed in the main text on every control volume. In particular, the first equation is Gauss's law of electrodynamics. The second equation constitutes a balance law for the electrons. The densities in each control volume change only due to in- and outflow through the boundary.

Next, the surface integrals are split into the sum of integrals over the planar interfaces between the control volume ω_k and its neighbors. Employing one point quadrature rules for the surface

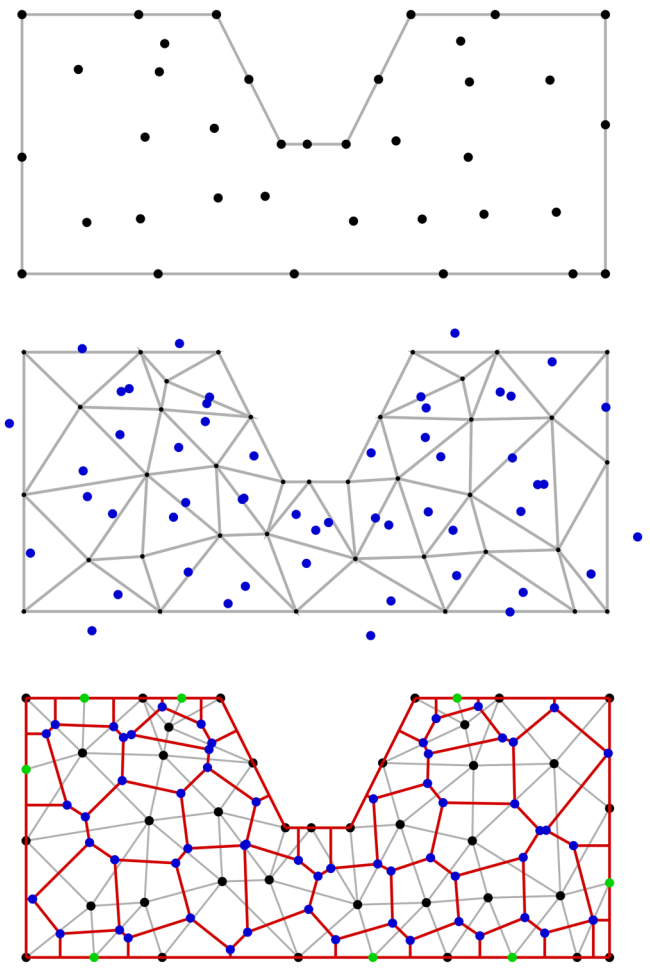

FIG. 9. First row: Piecewise linear description of computational domain with a given point cloud (black dots). Middle row: Delaunay triangulation of domain (gray edges) and triangle circumcenters (blue dots). As some boundary triangles have angles larger than 90° opposite to the boundary, their circumcenters lie outside of the domain. Last row: Boundary-conforming Delaunay triangulation with automatically inserted additional points at the boundary (green dots) by projecting the circumcenters outside onto the boundary of the computational domain. The boundary-conforming Delaunay triangulation is created from the original point cloud (black dots) plus the projected circumcenters (green dots). Now, all circumcenters (blue dots) lie within the computational domain. The boundaries of the (restricted) Voronoi cells are shown as well (red edges). Since the Voronoi cells are constructed from a boundary-conforming Delaunay triangulation, the edge between any two neighboring boundary cells is perpendicular to both boundary nodes. This is by construction also true for interior nodes and the edge separating them. The images were created with triangle.[49]

and volume integrals, we deduce the finite-volume scheme,

$$\begin{aligned}\sum_{\omega_\ell \in \mathcal{N}(\omega_k)} |\partial\omega_k \cap \partial\omega_\ell| D_{k,\ell} &= q|\omega_k|\big(C_k - n\big(\psi_k, \varphi_{n;k}\big)\big),\\ \sum_{\omega_\ell \in \mathcal{N}(\omega_k)} |\partial\omega_k \cap \partial\omega_\ell| j_{n;k,\ell} &= 0.\end{aligned} \tag{A1}$$

In the above formulas, $\mathcal{N}(\omega_k)$ denotes the set of all control volumes neighboring ω_k. In 2D, the measure $|\partial\omega_k \cap \partial\omega_\ell|$ corresponds to the length of the boundary line segment and in 3D to the area of the intersection of the boundary surfaces. The measure $|\omega_k|$ is in 2D given by the area and in 3D by the volume of the control volume ω_k. The unknowns ψ_k and $\varphi_{n;k}$ are approximations of the electric potential as well as the quasi Fermi potentials for electrons evaluated at node $\mathbf{x}_k$. The doping is defined by the integral average

$$C_k = \frac{1}{\omega_k}\int_{\omega_k} C(\mathbf{x})\, d\mathbf{x},$$

which can be approximated by its nodal value $C(\mathbf{x}_k)$. The numerical fluxes $D_{k,\ell}$ and $j_{n;k,\ell}$ in Eq. (A1) approximate the fluxes $-\varepsilon\nabla\psi \cdot \boldsymbol{\nu}_{k\ell}$ and $\mathbf{j}_n \cdot \boldsymbol{\nu}_{k\ell}$ in Eq. (4), respectively, on the interfaces between two adjacent control volumes ω_k and ω_ℓ. ψ_k, $\varphi_{n;k}$ and ψ_ℓ, $\varphi_{n;\ell}$.

While the electron flux is numerically approximated via an extension of the Scharfetter–Gummel scheme, Eq. (7), which can handle a spatially varying band-edge profile E_c^{dd}, the electric displacement flux is approximated by

$$D_{k,\ell} = -\varepsilon_s \frac{\psi_\ell - \psi_k}{h_{k,\ell}},$$

where

$$h_{k,\ell} = \|\mathbf{x}_\ell - \mathbf{x}_k\|$$

is the edge length. We point out that the flux approximation in Eq. (A1) is crucial to obtain a stable and physics preserving numerical solution.

DATA AVAILABILITY

The data that support the findings of this study are available from the corresponding author upon reasonable request.

REFERENCES

[1]C. J. Humphreys, MRS Bull. **33**, 459 (2008).
[2]M. Kneissl, T.-Y. Seong, J. Han, and H. Amano, Nat. Photonics **13**, 233 (2019).
[3]C.-Y. Yeh, Z. W. Lu, S. Froyen, and A. Zunger, Phys. Rev. B **46**, 10086 (1992).
[4]S. Strite and H. Morkoc, J. Vac. Sci. Technol. B **10**, 1237 (1992).
[5]H. Morkoc, S. Strite, G. B. Gao, M. E. Lin, B. Sverdlov, and M. Burns, J. Appl. Phys. **76**, 1363 (1994).
[6]F. Bernardini, V. Fiorentini, and D. Vanderbilt, Phys. Rev. B **56**, R10024 (1997).
[7]J. S. Im, H. Kollmer, J. Off, A. Sohmer, F. Scholz, and A. Hangleiter, Phys. Rev. B **57**, R9435 (1998).
[8]D. P. Williams, S. Schulz, A. D. Andreev, and E. P. O'Reilly, J. Sel. Top. Quantum Electron. **15**, 1092 (2009).
[9]O. Ambacher, J. Majewski, C. Miskys, A. Link, M. Hermann, M. Eickhoff, M. Stutzmann, F. Bernardini, V. Fiorentini, V. Tilak *et al.*, J. Phys.: Condens. Matter **14**, 3399 (2002).
[10]D. P. Williams, A. D. Andreev, E. P. O'Reilly, and D. A. Faux, Phys. Rev. B **72**, 235318 (2005).
[11]M. A. Caro, S. Schulz, S. B. Healy, and E. P. O'Reilly, J. Appl. Phys. **109**, 084110 (2011).
[12]C. X. Ren, Mater. Sci. Technol. **32**, 418 (2016).
[13]K. Bulashevich, O. Khokhlev, I. Evstratov, and S. Karpov, in *Light-Emitting Diodes: Materials, Devices, and Applications for Solid State Lighting XVI*, edited by K. P. Streubel, H. Jeon, L.-W. Tu, and N. Linder (International Society for Optics and Photonics (SPIE), 2012), p. 152.
[14]P. McBride, Q. Yan, and C. Van de Walle, Appl. Phys. Lett. **105**, 083507 (2014).
[15]D. Browne, B. Mazumder, Y.-R. Wu, and J. Speck, J. Appl. Phys. **117**, 185703 (2015).
[16]C.-K. Li, M. Piccardo, L.-S. Lu, S. Mayboroda, L. Martinelli, J. Peretti, J. S. Speck, C. Weisbuch, M. Filoche, and Y.-R. Wu, Phys. Rev. B **95**, 144206 (2017).
[17]S. Schulz, M. A. Caro, C. Coughlan, and E. P. O'Reilly, Phys. Rev. B **91**, 035439 (2015).
[18]D. Watson-Parris, M. J. Godfrey, P. Dawson, R. A. Oliver, M. J. Galtrey, M. J. Kappers, and C. J. Humphreys, Phys. Rev. B **83**, 115321 (2011).
[19]T.-J. Yang, R. Shivaraman, J. S. Speck, and Y.-R. Wu, J. Appl. Phys. **116**, 113104 (2014).
[20]D. N. Arnold, G. David, D. Jerison, S. Mayboroda, and M. Filoche, Phys. Rev. Lett. **116**, 056602 (2016).
[21]M. Filoche, M. Piccardo, Y.-R. Wu, C.-K. Li, C. Weisbuch, and S. Mayboroda, Phys. Rev. B **95**, 144204 (2017).
[22]D. Chaudhuri, J. C. Kelleher, M. R. O'Brien, E. P. O'Reilly, and S. Schulz, Phys. Rev. B **101**, 035430 (2020).
[23]D. Ferry, S. Ramey, L. Shifren, and R. Akis, J. Comput. Electron. **1**, 59 (2002).
[24]D. A. Zakheim, A. S. Pavluchenko, D. A. Bauman, K. A. Bulashevich, O. V. Khokhlev, and S. Y. Karpov, Phys. Status Solidi A **209**, 456 (2012).
[25]F. Roemer and B. Witzigmann, Opt. Quantum Electron. **50**, 1 (2018).
[26]J. Geng, P. Sarangapani, K.-C. Wang, E. Nelson, B. Browne, C. Wordelman, J. Charles, Y. Chu, T. Kubis, and G. Klimeck, Phys. Status Solidi A **215**, 1700662 (2018).
[27]M. O'Donovan, M. Luisier, E. P. O'Reilly, and S. Schulz, J. Phys.: Condens. Matter **33**, 045302 (2021).
[28]A. Di Vito, A. Pecchia, A. Di Carlo, and M. Auf Der Maur, J. Appl. Phys. **128**, 041102 (2020).
[29]D. Chaudhuri, M. O'Donovan, T. Streckenbach, S. K. P. O. Marquardt, P. Farrell, T. Koprucki, and S. Schulz, J. Appl. Phys. **129**, 073104 (2021).
[30]J.-R. Chen, S.-C. Ling, H.-M. Huang, P.-Y. Su, T. Ko, T.-C. Lu, H.-C. Kuo, Y.-K. Kuo, and S.-C. Wang, Appl. Phys. B **95**, 145 (2009).
[31]C.-S. Xia, Z. M. S. Li, W. Lu, Z. H. Zhang, Y. Sheng, and L. W. Cheng, Appl. Phys. Lett. **99**, 233501 (2011).
[32]M. A. Caro, S. Schulz, and E. P. O'Reilly, Phys. Rev. B **88**, 214103 (2013).
[33]S. J. Plimpton, J. Comput. Phys. **117**, 1 (1995).
[34]D. S. P. Tanner, P. Dawson, M. J. Kappers, R. A. Oliver, and S. Schulz, Phys. Rev. Appl. **13**, 044068 (2020).
[35]H. Si, ACM Trans. Math. Software **41**, 1 (2015).
[36]H. Si, TetGen version 1.5; see http://tetgen.org/ (accessed December 1, 2015).
[37]D. H. Doan, P. Farrell, J. Fuhrmann, M. Kantner, T. Koprucki, and N. Rotundo, see http://doi.org/10.20347/WIAS.SOFTWARE.DDFERMI for "ddfermi—A Drift-Diffusion Simulation Tool," Weierstrass Institute (WIAS), 2020.
[38]J. Fuhrmann, T. Streckenbach *et al.*, "pdelib: A finite volume and finite element toolbox for PDEs," pdelib version 2.4.20190405, Weierstrass Institute (WIAS), 2019; see http://pdelib.org.
[39]D. Braess, *Finite Elemente* (Springer, Berlin, 1997); see https://doi.org/10.1007/978-3-662-07233-2.

[40]J. W. Barrett and C. M. Elliott, Numer. Math. **49**, 343 (1986).
[41]O. Schenk, PARDISO version 5.0.0; see http://www.pardiso-project.org (accessed February 22, 2016).
[42]D. N. Arnold, G. David, M. Filoche, D. Jerison, and A. Mayboroda, SIAM J. Sci. Comput. **41**, B69 (2019).
[43]P. Farrell, N. Rotundo, D. H. Doan, M. Kantner, J. Fuhrmann, and T. Koprucki, in *Handbook of Optoelectronic Device Modeling and Simulation*, edited by J. Piprek (CRC Press, 2017), Vol. 2, Chap. 50, pp. 733–771.
[44]W. Van Roosbroeck, Bell Syst. Tech. J. **29**, 560 (1950).
[45]M. Ilegems and H. Montgomery, J. Phys. Chem. Solids **34**, 885 (1973).
[46]M. E. Levinshtein, S. L. Rumyantsev, and S. Shur Michael, *Properties of Advanced Semiconductor Materials* (Wiley & Sons, 2001).
[47]D. L. Scharfetter and H. K. Gummel, IEEE Trans. Electron Devices **16**, 64 (1969).
[48]F. Massabuau, N. Piot, M. Frentrup, X. Wang, Q. Avenas, M. Kappers, C. Humphreys, and R. Oliver, Phys. Status Solidi B **254**, 1600664 (2017).
[49]J. Shewchuk, "Triangle: A two-dimensional quality mesh generator and Delaunay triangulator"; see http://www.cs.cmu.edu/~quake/triangle.html (accessed December 1, 2015).